

Supporting Information to:  
Nanosecond Solvation Dynamics of the Hematite/Liquid  
Water Interface at Hybrid DFT Accuracy Using Committee  
Neural Network Potentials

Philipp Schienbein<sup>\*1</sup> and Jochen Blumberger<sup>11</sup>

<sup>1</sup>Department of Physics and Astronomy, University College London, London,  
WC1E 6BT, United Kingdom

\*email: p.schienbein@ucl.ac.uk

<sup>1</sup>email: j.blumberger@ucl.ac.uk

## Contents

<b>S1 Electronic Structure Setup</b>	<b>2</b>
<b>S2 Validation of the Committee Neural Network Potential</b>	<b>2</b>
<b>S3 Simulation Boxes</b>	<b>2</b>
<b>S4 Temperature dependence of the dynamics of HSE06-D3 bulk liquid water</b>	<b>4</b>
<b>S5 Finite-size effects of the self-diffusion coefficient</b>	<b>6</b>
<b>S6 Reactant and Product State Definitions for Determining Residence Times</b>	<b>7</b>
<b>S7 H-bond Definition</b>	<b>8</b>

## S1 Electronic Structure Setup

All electronic structure calculations have been carried out using `Quickstep` implemented in version 8.1 of the `CP2k` software suite [1]. The HSE06 hybrid density functional [2] with 12 % Hartree-Fock exchange (which was found to be ideal for hematite [3]) supplemented by D3 dispersion corrections [4] has been used. To represent the valence electrons, a mixed Gaussian/plane wave basis set is used [5], where we used a triple- $\zeta$  quality basis set for the H atoms, double- $\zeta$  quality basis set for the Fe, and O atoms and a kinetic energy cutoff of 600 Ry for the plane wave basis set. Core electrons are represented by norm-conserving relativistic Goedecker-Teter-Hutter (GTH) pseudo potentials [6, 7]. This electronic structure setup follows the one used previously [8].

## S2 Validation of the Committee Neural Network Potential

To ensure that the conducted simulations based on the trained c-NNP are meaningful, its results need to be verified. In their latest publication [11], Schran et al. introduced a scoring scheme which can be used to quantify the agreement of the c-NNP with the underlying full ab initio reference. Within this scoring scheme, the structure, velocities, and forces are validated in terms of the respective radial distribution functions (RDFs), velocity density of states (VDOS) and one-to-one comparison of the forces. Here it is important to realize that the RDFs are converged quite quickly, such that the highest scores are expected for this property, while the forces are relatively difficult to train, such that this is the most important criterion. To validate the NNP forces, we randomly extract 20 configurations from a c-NNP MD simulation and computed the explicit ab initio forces with `cp2k`. Importantly, the force validation is performed against configurations which have *not* been included into the training set of the c-NNP. Note that we could not compare the VDOS with the existing ab initio trajectories because for the previous publication [8] many short trajectories have been generated which are too short to obtain a statistically meaningful VDOS.

In Fig. S1a we compare all possible RDF combinations obtained from the full AIMD simulation data from Ref. [8] with the ones obtained from the c-NNP simulations. By inspecting the figure, one can see that there is almost no difference between the c-NNP and the full AIMD structure. Using the scoring scheme to quantify the agreement of the RDF [11], we obtain a score of 97.34 % for the RDFs. In Fig. S1b the density profile as a function of distance from the nearest hematite surface is shown. We observe that the agreement between the c-NNP and the AIMD data is qualitatively good: The peak positions are all correctly reproduced by the c-NNP, only the height of the density graph shows some quantitative difference. Note, however, that the available AIMD data is not sufficient to obtain fully converged graphs and therefore the comparison is quite difficult. This figure gives a hint already that the trained c-NNP is indeed a useful tool to fully converge structural and dynamical properties. In Fig. S1c we present the comparison between the AIMD and c-NNP forces of the 20 randomly selected test structures, see above. Again, we observe a fairly good agreement between the two different ways to obtain the atomic forces, but there are some outliers. Using the scoring scheme [11], we obtain an overall score of 84.35 % for the forces. In total, the obtained scorings for the RDF and the forces as well as the overall force RMSE are in good agreement to the previous published c-NNPs [11]. Therefore, our trained c-NNP are indeed capable to reproduce the hematite/water system at the level of hybrid DFT.

## S3 Simulation Boxes

In our previous work [8], we used NpT simulations with a flexible simulation cell containing 93 water molecules. Here, we took a single snapshot from those equilibrated NpT simulations, illustrated in Fig. S2, with the cell dimensions  $a = 10.241 \text{ \AA}$ ,  $b = 10.2943 \text{ \AA}$ ,  $c = 47.3423 \text{ \AA}$ ,  $\alpha = 91.966^\circ$ ,  $\beta = 87.424^\circ$ , and  $\gamma = 119.738^\circ$ . From this cell, we extended the  $c$  axis, being perpendicular to the hematite slab, to  $80 \text{ \AA}$  and inserted as many water molecules as necessary to keep the experimental water density of  $0.997 \text{ kg L}^{-1}$ . This cell was then taken as “unit cell” for further trivial box size increments along the axes parallel to the hematite slab which can be achieved by multiplying the unit cell along the  $a$  or  $b$  axes. All employed system sizes are summarized in Table 1. As long as not reported differently, all reported results in the main text are based on the “(2x2)” box because it

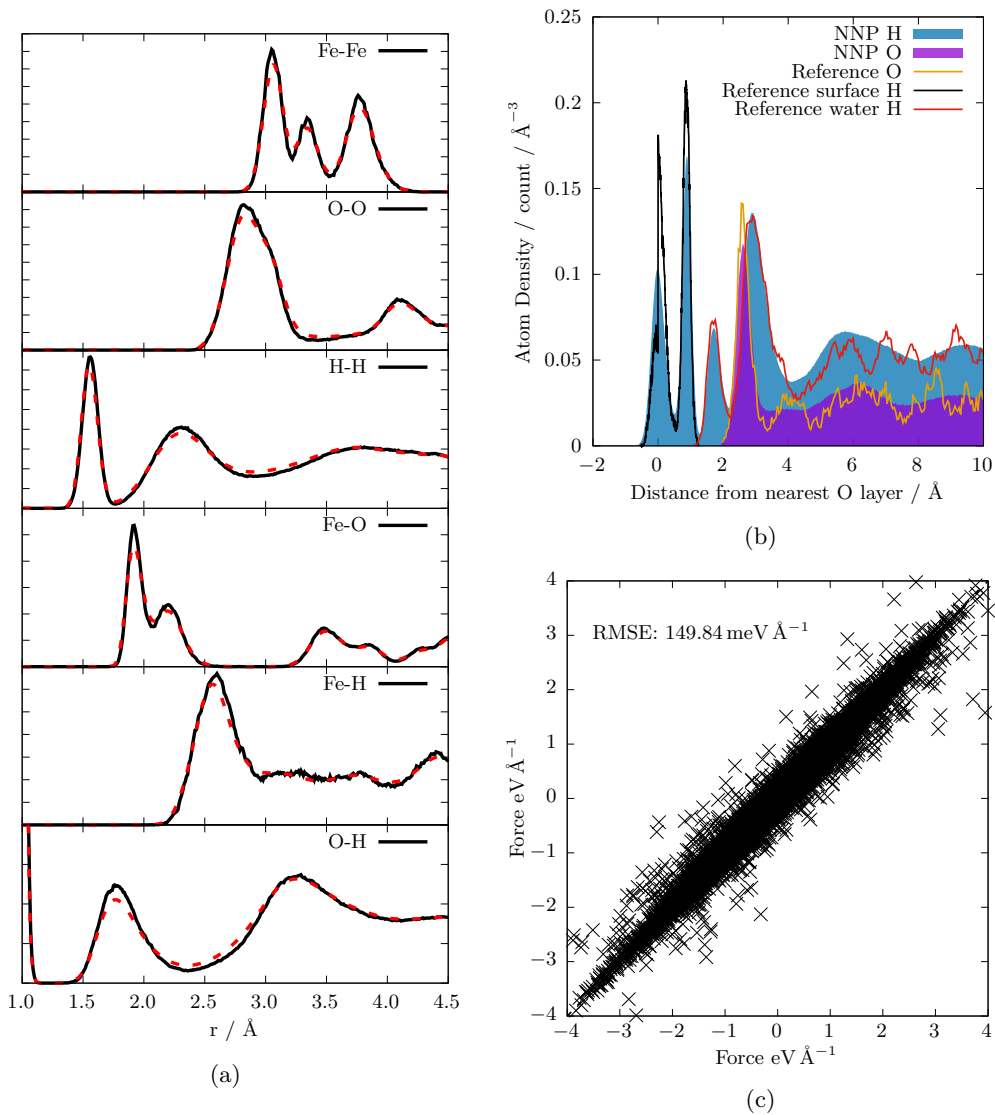
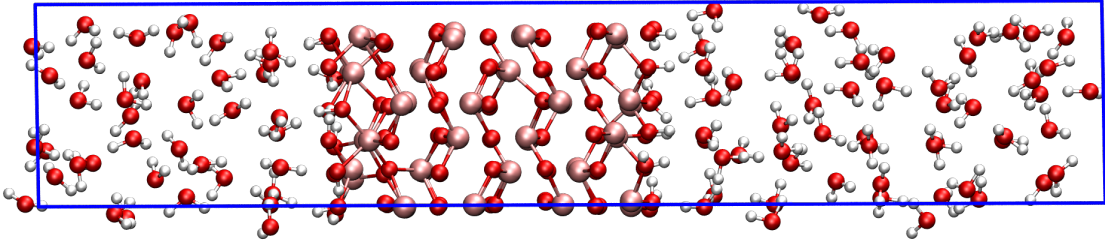


Figure S1: Assessment of the quality of the trained c-NNP on describing the hematite/liquid water interface, in terms of all possible RDF combinations (a), the atom density as a function of distance to the nearest hematite surface (b), and a direct comparison of the c-NNP with the AIMD force (c). In (a), the red dashed and the solid black lines show the RDFs obtained from c-NNP and AIMD simulations, respectively. In (b) the filled curves depict the hydrogen (blue) and oxygen (purple) densities obtained from c-NNP simulations, while the solid lines show the oxygen hydrogen (black), water hydrogen (red) and water oxygen (orange) atom densities from AIMD simulations. The AIMD data in (a) and (b) is taken from our previous publication [8]. Note that the distributions based on these AIMD simulations are not fully converged yet. In (c) we show a one to one force comparison between c-NNP and explicit ab initio calculations. Here, the ab initio forces were computed from 20 randomly selected configurations which have *not* been included into the training set. Note that similar force RMSEs have been reported in previous publications, e.g. for liquid water at a Cu slab ( $207.5 \text{ meV } \text{Å}^{-1}$ ) [9],  $\text{Li}_x\text{Mn}_2\text{O}_4$  [10] ( $240.0 \text{ meV } \text{Å}^{-1}$ ) or liquid water at  $\text{MoS}_2$  slabs [11] ( $190.1 \text{ meV } \text{Å}^{-1}$ ).

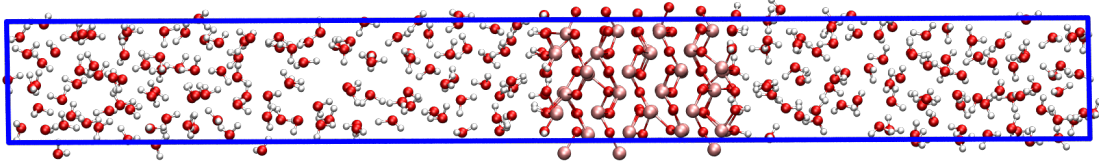
contains the most particles and therefore provides the best statistical quality among the employed boxes.

Table 1: Hematite/Water simulation box sizes employed in this work, where  $a$ ,  $b$ , and  $c$  give the respective length of the lattice vectors,  $N_{\text{atoms}}$  is the number of atoms in the simulation box and  $N_{\text{wat}}$  is the number water molecules in the simulation box. For all boxes, the same angles between the lattice vectors have been used, namely  $\alpha = 91.966^\circ$ ,  $\beta = 87.424^\circ$ , and  $\gamma = 119.738^\circ$ . The “(47 Å)” box has been taken from our previous hematite/Water simulations [8].

	$a/\text{\AA}$	$b/\text{\AA}$	$c/\text{\AA}$	$N_{\text{atoms}}$	$N_{\text{wat}}$
“(47 Å)”	10.241	10.2943	47.3423	435	93
“(80 Å)”	10.241	10.2943	80	780	208
“(1x2)”	10.241	20.5886	80	1560	416
“(2x2)”	20.482	20.5886	80	3120	832



(a)



(b)

Figure S2: View of the (47 Å) (a) and (80 Å) (b) simulation boxes along the  $b$  axis, see Table 1. H, O, and Fe atoms are colored in white, red and beige, respectively. For reference, the unit cell is depicted with blue solid lines.

## S4 Temperature dependence of the dynamics of HSE06-D3 bulk liquid water

For our previous simulation of the hematite/liquid Water interface [8] we opted to use an effective simulation temperature of 330 K to correctly model liquid ambient water. This higher effective simulation temperature has regularly been used in the context of interfaces between liquid water and other metal oxide materials, e.g.  $\text{TiO}_2$  [12]. The HSE06 hybrid functional is derived from the GGA functional PBE, such that it uses the very same exchange and correlation terms at its parent functional, but mixes the PBE exchange with exact HF exchange. Therefore it is expected that the HSE06 functional behaves qualitatively similar to its parent functional PBE. Indeed, it was shown that the structure of liquid water (in terms of the OO and OH RDF) of the HSE06 functional does not significantly differ from PBE [13]. Note that the original HSE06 functional adds 25 % HF exchange, while we only use 12 % HFX. While this certainly changes the functional, it renders our HSE06 even more similar to the parent PBE functional since it is changed less compared to the latter. Importantly, it is well known from the literature, that the PBE functional tends to overbind intermolecular water–water interactions [14]. Here it could be shown that an even higher effective temperature of 400 K is required to get the structure *and* dynamics (in terms of the self-diffusion coefficient) right. Note that the same overbinding effect could also be seen for the hybrid PBE0 functional [15] which is also derived from the PBE functional. This undeniably high effective simulation temperature has successfully been employed in the literature, e.g. to simulate aqueous

ion solutions with the PBE GGA functional [16] or with the hybrid PBE0 functional [17].

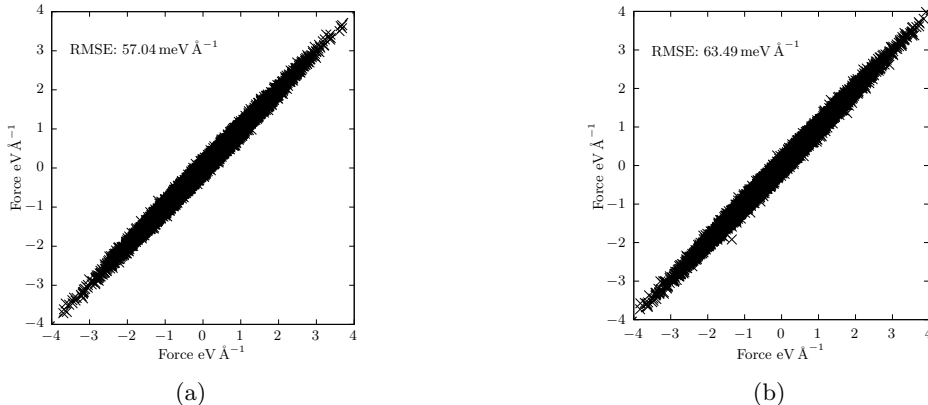


Figure S3: Assessment of the c-NNP trained for the hematite/liquid water interface on describing pure bulk liquid water at 330 (a) and 400 K (b) only. Here we compare the calculated c-NNP forces with the explicit ab initio forces, where the latter have been calculated from 20 randomly drawn configurations from the c-NNP simulation.

Using our trained c-NNP we can also run simulations on bulk liquid water since the hematite/liquid water box contains a sufficiently large bulk water region. Using the c-NNP we can therefore set out to assess the temperature dependence of the hybrid HSE06-D3 functional. To ensure that bulk liquid water is indeed reproduced correctly at the level of HSE06-D3 by our c-NNP, we did a careful validation. First of all, we conducted NVT simulations of bulk liquid water at 330 and 400 K using the c-NNP and again randomly selected 20 configurations. For all these 20 configurations we calculated the explicit ab initio forces at the HSE06-D3 level of theory using the setup described in Sec. S1. We then compared the resulting forces as shown in Fig. S3, computed the RMSE, and the score [11]. For bulk liquid water at 330 and 400 K we obtain a force score of 92.76 and 92.75 % , respectively. Therefore, the overall agreement between the explicit ab initio calculation and the c-NNP is very good, proving that we can use the latter to simulate bulk liquid water at the given temperatures.

In Fig. S4a we show the RDF of HSE06-D3 water from a bulk liquid water simulation using the trained c-NNP introduced above as a function of temperature. Moreover, we also plot the experimental reference data as obtained by joint Neutron and X-Ray diffraction experiments [18]. We observe that the agreement with the experimental reference becomes better with increasing temperatures. This finding is in agreement with previous results using the PBE GGA functional [14]. In Fig. S4b we plot the diffusion coefficient of bulk liquid water using the trained c-NNP as a function of system size. Using this plot, the finite-size corrected diffusion coefficient can be extrapolated, see below. Here we find that the finite-size corrected diffusion coefficient at 330 K is  $0.49 \times 10^{-5} \text{ cm}^2 \text{ s}^{-1}$  which is about one order of magnitude smaller than the experimental value determined by NMR measurements [19] of  $2.61 \times 10^{-5} \text{ cm}^2 \text{ s}^{-1}$  at 300 K. Instead, our determined diffusion coefficient at 330 K agrees very well with simulation data of liquid water using the similar PBE functional [14] at 349 K of  $0.33 \times 10^{-5} \text{ cm}^2 \text{ s}^{-1}$ . These findings for the RDF and the diffusion coefficient indeed underline that the hybrid HSE06-D3 functional using 12 % HFX suffers from the same systematic overbinding of intermolecular interactions in liquid water which are well documented already [14]. At 365 and 400 K we computed finite-size corrected self diffusion coefficients of  $1.57 \times 10^{-5}$  and  $3.41 \times 10^{-5} \text{ cm}^2 \text{ s}^{-1}$ , respectively, where the former is somewhat smaller and the latter is somewhat larger than the experimental value. Recall that, the structural properties in terms of the RDF agree much better with the experimental reference data compared to the lower simulation temperatures. Therefore we opt to use 400 K as effective simulation temperature throughout this paper because it seems to be a good compromise to get both, the structure and dynamics of liquid water at the hematite interface at ambient conditions sufficiently right.

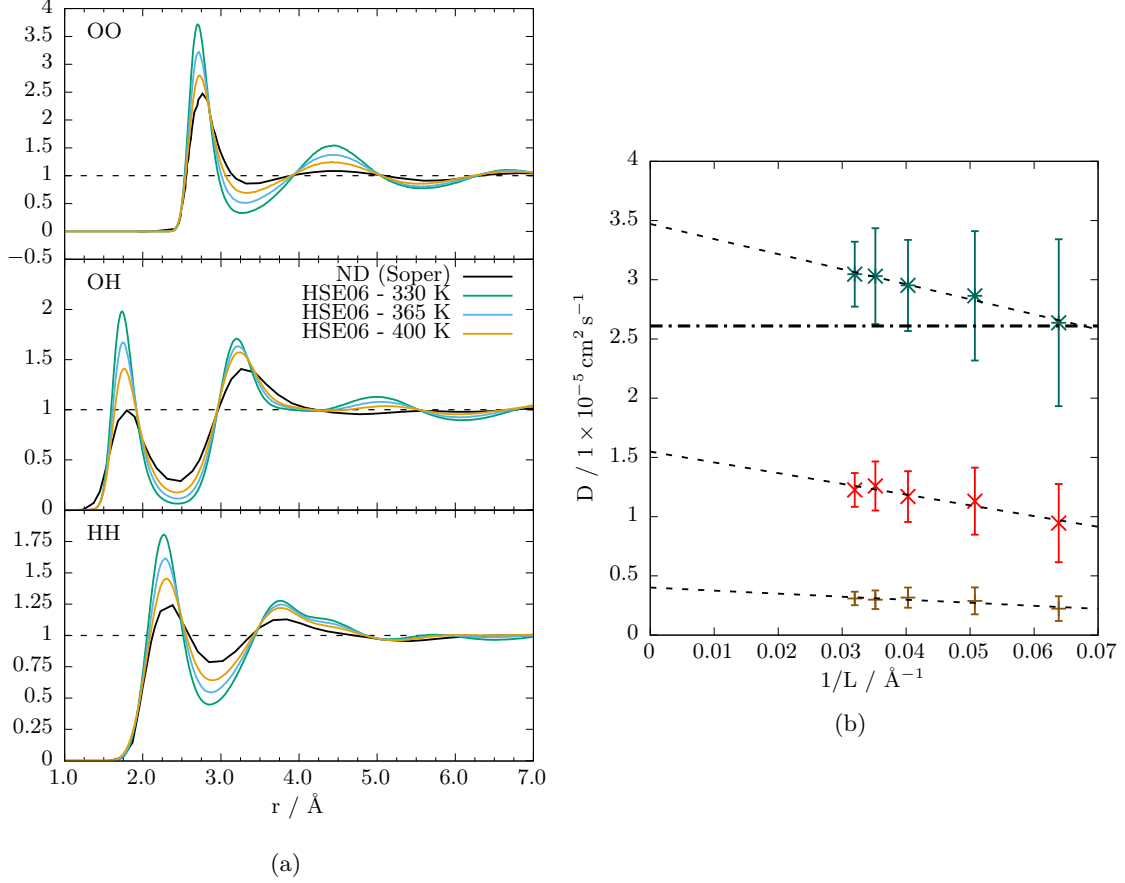


Figure S4: Comparison of the structural and dynamical properties of HSE06-D3 water in terms of their RDF (a) and self diffusion coefficients (b) as a function of temperature at 330 (green), 365 (blue), and 400 K (orange). For reference, the respective RDFs obtained from a joint analysis of available ND and XRD measurements [18] at 300 K are also shown (black solid lines). The underlying simulations to obtain the graphs have been obtained using the c-NNP trained for the hematite/liquid water interface applied to bulk liquid water only. The intercept of the linear fits in (b) yields the finite-size corrected diffusion coefficient. Note that the self diffusion coefficient in liquid water at 300 K was measured to be  $2.61 \times 10^{-5} \text{ cm}^2 \text{ s}^{-1}$  by NMR experiments [19] which is illustrated as black dashed-dotted horizontal line in (b).

## S5 Finite-size effects of the self-diffusion coefficient

Finite size effects for isotropic, cubic simulation boxes are quite well known and studied [20, 21]. Therein, a correction equation was derived to estimate the magnitude of the finite size effects and to extrapolate the results to an infinitely large box. The self-diffusion coefficient of an infinitely large simulation box

$$D_0 = D_{\text{PBC}} - \frac{2.837k_{\text{B}}T}{6\pi\eta L} \quad (\text{S1})$$

can therein be calculated from the finite-size dependent value,  $D_{\text{PBC}}$ , where  $k_{\text{B}}$  is the Boltzmann constant,  $T$  is the temperature,  $L$  is the length of the cubic simulation cell, and  $\eta$  is the viscosity. The viscosity can be computed from the simulation via the stress tensor [22]. Alternatively, the self-diffusion coefficient can be extrapolated from linear regression of multiple system sizes. Here, we computed  $D_{\text{PBC}}$  from five different system sizes, namely 128, 256, 512, 768, and 1024 water molecules at 330, 365, and 400 K. Cubic simulation boxes and a density of  $0.997 \text{ kg L}^{-1}$  have been used throughout. The results are shown in Fig. S4b. We find a finite size corrected self-diffusion coefficient for liquid water of  $0.49 \times 10^{-5}$ ,  $1.57 \times 10^{-5}$ , and  $3.41 \times 10^{-5} \text{ cm}^2 \text{ s}^{-1}$  at 330, 365, and 400 K, respectively. From the slope of the linear fits,  $\eta\beta = \eta/k_{\text{B}}T$  can be estimated as a function

of effective simulation temperature. Recall, that we are using an effective simulation temperature of 400 K to mimic ambient liquid water using the HSE06-D3 functional, see above. At 400 K we find  $\eta\beta = 1606.80 \text{ s cm}^{-2} \text{ \AA}^{-1}$ . This value will be used below, to estimate the finite-size correction within the hematite/Water box.

In case of a system being confined in one dimension, finite size corrections have also been introduced recently [23]. In such systems, the self-diffusion coefficient (as given by Einstein or Green-Kubo relations) is only meaningfully defined in the direction parallel to the confining surface. Moreover, the self-diffusion coefficient in that direction necessarily depends on the height of the simulation box,  $H$ , i.e. the distance between the confining surfaces. In cases where  $H$  is larger than the square surface area length  $L$  the authors introduced a finite size correction

$$\Delta D^{\parallel}(H > L) = \frac{1}{\eta\beta} \left[ \frac{3}{40} \frac{H}{L^2} - \frac{3 \ln(1 + \sqrt{2})}{4\pi L} \right], \quad (\text{S2})$$

and the self-diffusion coefficient for an infinitely large box

$$D_0^{\parallel}(H) = D_{\text{PBC}}^{\parallel}(H) - \Delta D^{\parallel}(H > L) \quad (\text{S3})$$

can be extrapolated. Note that, the hematite/Water simulation boxes are approximately squared, see Table 1.

Generally, one can again increase the system size systematically to obtain a fit and thereby extrapolate  $D_0^{\parallel}$ , as we did it for bulk water, see above. However, even with the c-NNP, this is not easily possible because the system size of the hematite/water box cannot arbitrarily be increased, but just by integer factors of the unit cell. Moreover, the extrapolation equation also requires the surface area to be a square, therefore for each larger system size, the total number of atoms increases by a factor of 4. This quickly results in simulation boxes containing more than 10,000 atoms and would result in a huge amount of data. Instead of doing this extrapolation, we now take the determined  $\eta\beta$  from the bulk water simulations at the same temperature. This way also guarantees that the temperature is correctly taken into account because  $\eta\beta$  was determined from the very same effective simulation temperature. Note that it is assumed that  $\eta$  does not change as a function of system size (otherwise the finite-size extrapolation equations given above would also not work). This has also been confirmed, see e.g. [22]. The finite-size corrected self-diffusion coefficients of water confined between the two hematite slabs are shown in Fig. 5 in the main text.

## S6 Reactant and Product State Definitions for Determining Residence Times

The calculation of residence lifetimes, as described in Eq. 1 in the main text, requires the definition of reactant and product states. In case of a water molecule leaving the first solvation layer at the hematite interface, the geometrical definitions of the reactant and product states are illustrated in Fig. S5. The figure shows the logarithm of the O atom density (only of water molecules) as a function of distance from the hematite surface. The logarithm is taken, since it can then be interpreted as an effective mean field potential (in full analogy to a radial distribution function [24]) being helpful for the discussion. Within the stable state picture (SSP) [25], recrossings of the transition state are not counted as “reactive” trajectories. Therefore, reactant and product states must be chosen deeply into their respective energy minima, i.e. settled. This means that at  $t = 0$ , the water molecule must be located deeply in the energy minimum in the first solvation layer (reactant state) to be considered for analysis. Moreover, the trajectory of that water molecule is only counted “reactive” if it reaches the minimum of the product state (second solvation layer). Thereby the probability that the water molecule immediately returns back to the reactive state (“recrossing”) is minimized.

To obtain the kinetics of the in-plane/out-of-plane dynamics of the terminal OH groups at the hematite slab, we used the same technique as for the first layer residence time. The geometrical definition of the product and reactant states are illustrated in Fig. S6. Note that in this case both paths of the transition are taken into account, i.e. the transition from a parallel to a perpendicular

arrangement and vice-versa. In the former case, the “parallel state” is the reactant and the “perpendicular state” is the product. For the backward transition, the definition of the reactant and product states are exactly opposite.

## S7 H-bond Definition

H-bonds are defined using the joint-angle criterion

$$r_{\text{HO}} < c_1^{\text{HO}} + c_2^{\text{HO}} \cos \Theta, \quad (\text{S4})$$

where  $r_{\text{HO}}$  is the intermolecular  $\text{O} \cdots \text{H}$  distance and  $\Theta$  is the corresponding  $\text{O} \cdots \text{H}-\text{O}$  angle. Within this definition,  $\cos \Theta = -1$  corresponds to a perfectly linear H-bond arrangement. The two parameters  $c_1^{\text{HO}}$  and  $c_2^{\text{HO}}$  can be determined from joint angle-distance distribution functions (JDF). Values of  $c_1^{\text{HO}} = 1.37 \text{ \AA}$  and  $c_2^{\text{HO}} = -1.71 \text{ \AA}$  have been shown to be useful for liquid ambient water in general [26, 16, 27, 28]. For bulk HSE06 water, simulated by our c-NNP, the JDF is shown in Fig. S7 including the H-bond criterion. As one can see, the employed criterion cuts through the saddle point between perfectly linear H-bonded pairs at  $r_{\text{OH}} \approx 1.8 \text{ \AA}$  and  $\cos \Theta = -1$  and non H-bonded  $\text{O} \cdots \text{H}$  configurations. Note that this H-bond definition also belongs to the so-called  $r$ - $\alpha$  definitions of H-bonds [29].

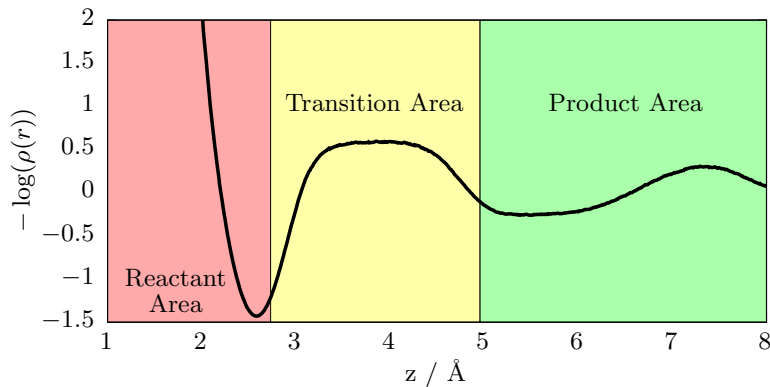


Figure S5: Negative logarithm of the density profile of O atoms belonging to water molecules as a function of distance from the hematite interface. This quantity can be interpreted as an effective mean potential in full analogy to the radial distribution function [24]. At  $z = 0$  the top-most oxygen layer of the hematite interface is located, see also Fig. 1 in the main text. The red, yellow, and green colors indicate those distances, where the water molecule is counted to be in the reactant, transition, and product states, respectively. Specifically, a water molecule is counted to be in the reactant or product states, if the distance of the corresponding O atom from the average location of the topmost O layer of the hematite slab is smaller than 2.73 or larger than 4.96 Å, respectively.

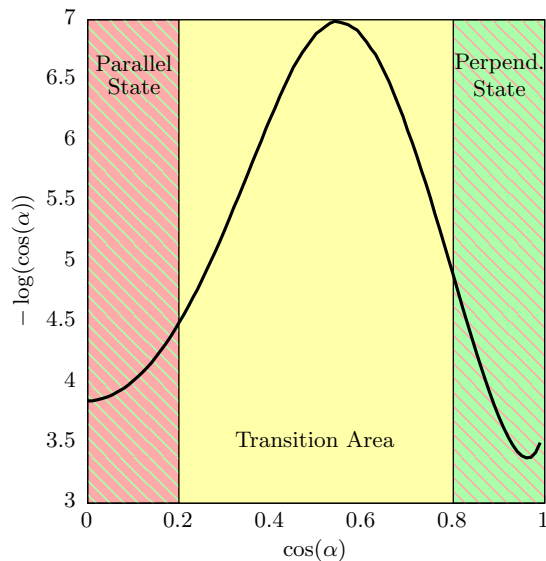


Figure S6: Negative logarithm of the angular distribution function of the angle between the bond vector of terminal OH groups and the hematite surface normal. Therefore the cosine of one indicates a perpendicular arrangement, whereas a cosine of zero indicates that the OH group is oriented parallel to the hematite surface plane. As in Fig. S5, the yellow area depicts the transition state between the reactant and product states. Since we take the forward and backward reactions into account, the reactant state (red) and product state (green) can be interchanged indicated by the shaded background. Again, the negative logarithm can be interpreted as a kind of effective mean potential in full analogy to radial distribution functions [24].

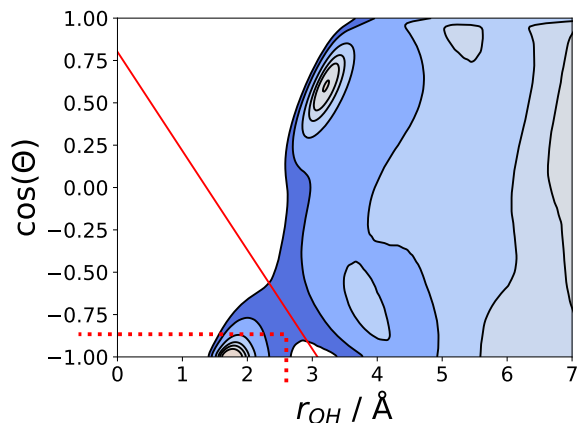


Figure S7: H-bonding structure of HSE06-D3 water as modeled using our trained c-NNP model, where  $r_{OH}$  gives the intermolecular  $O \cdots H$  distance and  $\Theta$  is the corresponding  $O \cdots H-O$  angle. A value of  $\cos \Theta = -1$  corresponds to a perfectly linear arrangement. The probability increases from blue to red colors, whereas white corresponds to zero probability. The individual contour levels are shown on a logarithmic scale. The employed geometric H-bond criterion employed in this work (see S4) is shown as red solid line. For comparison, the Luzar-Chandler H-bond criterion [30] (which has frequently been used in the literature) is shown using a dotted red line; there an intermolecular  $O \cdots H$  contact is counted as H-bond if  $r_{HO} < 2.6 \text{ \AA}$  and  $\Theta < 30^\circ$ .

## References

- [1] T. D. Kühne, M. Iannuzzi, M. D. Ben, V. V. Rybkin, P. Seewald, F. Stein, T. Laino, R. Z. Khaliullin, O. Schütt, F. Schiffmann, D. Golze, J. Wilhelm, S. Chulkov, M. H. Bani-Hashemian, V. Weber, U. Borštnik, M. TAILLEFUMIER, A. S. Jakobovits, A. Lazzaro, H. Pabst, T. Müller, R. Schade, M. Guidon, S. Andermatt, N. Holmberg, G. K. Schenter, A. Hehn, A. Bussy, F. Belleflamme, G. Tabacchi, A. Glöß, M. Lass, I. Bethune, C. J. Mundy, C. Plessl, M. Watkins, J. VandeVondele, M. Krack, and J. Hutter. “CP2K: An electronic structure and molecular dynamics software package - Quickstep: Efficient and accurate electronic structure calculations”. *J. Chem. Phys.* 152 (2020), p. 194103.
- [2] A. V. Krukau, O. A. Vydrov, A. F. Izmaylov, and G. E. Scuseria. “Influence of the exchange screening parameter on the performance of screened hybrid functionals”. *J. Chem. Phys.* 125 (2006), p. 224106.
- [3] Z. D. Pozun and G. Henkelman. “Hybrid density functional theory band structure engineering in hematite”. *J. Chem. Phys.* 134 (2011), p. 224706.
- [4] S. Grimme, J. Antony, S. Ehrlich, and H. Krieg. “A Consistent and Accurate Ab Initio Parametrization of Density Functional Dispersion Correction (DFT-D) for the 94 Elements H-Pu”. *J. Chem. Phys.* 132 (2010), p. 154104.
- [5] J. VandeVondele and J. Hutter. “Gaussian Basis Sets for Accurate Calculations on Molecular Systems in Gas and Condensed Phases”. *J. Chem. Phys.* 127 (2007), p. 114105.
- [6] S. Goedecker, M. Teter, and J. Hutter. “Separable Dual-Space Gaussian Pseudopotentials”. *Phys. Rev. B* 54 (1996), pp. 1703–1710.
- [7] C. Hartwigsen, S. Goedecker, and J. Hutter. “Relativistic Separable Dual-Space Gaussian Pseudopotentials from H to Rn”. *Phys. Rev. B* 58 (1998), pp. 3641–3662.
- [8] G. F. von Rudorff, R. Jakobsen, K. M. Rosso, and J. Blumberger. “Fast Interconversion of Hydrogen Bonding at the Hematite (001)–Liquid Water Interface”. *J. Phys. Chem. Lett.* 7 (2016), pp. 1155–1160.
- [9] S. K. Natarajan and J. Behler. “Neural network molecular dynamics simulations of solid–liquid interfaces: water at low-index copper surfaces”. *Phys. Chem. Chem. Phys.* 18 (2016), pp. 28704–28725.
- [10] M. Eckhoff and J. Behler. “Insights into lithium manganese oxide–water interfaces using machine learning potentials”. *J. Chem. Phys.* 155 (2021), p. 244703.
- [11] C. Schran, F. L. Thiemann, P. Rowe, E. A. Müller, O. Marsalek, and A. Michaelides. “Machine learning potentials for complex aqueous systems made simple”. *Proc. Natl. Acad. Sci. USA* 118 (2021).
- [12] J. Cheng and M. Sprik. “Acidity of the Aqueous Rutile TiO<sub>2</sub>(110) Surface from Density Functional Theory Based Molecular Dynamics”. *J. Chem. Theory Comput.* 6 (2010), pp. 880–889.
- [13] M. Guidon, F. Schiffmann, J. Hutter, and J. VandeVondele. “Ab initio molecular dynamics using hybrid density functionals”. *J. Chem. Phys.* 128 (2008), p. 214104.
- [14] E. Schwegler, J. C. Grossman, F. Gygi, and G. Galli. “Towards an assessment of the accuracy of density functional theory for first principles simulations of water. II”. *J. Chem. Phys.* 121 (2004), pp. 5400–5409.
- [15] C. Zhang, D. Donadio, F. Gygi, and G. Galli. “First Principles Simulations of the Infrared Spectrum of Liquid Water Using Hybrid Density Functionals”. *J. Chem. Theory Comput.* 7 (2011), pp. 1443–1449.

- [16] P. Schienbein, G. Schwaab, H. Forbert, M. Havenith, and D. Marx. “Correlations in the Solute–Solvent Dynamics Reach Beyond the First Hydration Shell of Ions”. *J. Phys. Chem. Lett.* 8 (2017), pp. 2373–2380.
- [17] A. P. Gaiduk, C. Zhang, F. Gygi, and G. Galli. “Structural and electronic properties of aqueous NaCl solutions from ab initio molecular dynamics simulations with hybrid density functionals”. *Chem. Phys. Lett.* 604 (2014), pp. 89–96.
- [18] A. K. Soper. “Joint structure refinement of x-ray and neutron diffraction data on disordered materials: application to liquid water”. *J. Phys.: Condens. Matter* 19 (2007), p. 335206.
- [19] K. Yoshida, C. Wakai, N. Matubayasi, and M. Nakahara. “A new high-temperature multinuclear-magnetic-resonance probe and the self-diffusion of light and heavy water in sub- and supercritical conditions”. *J. Chem. Phys.* 123 (2005), p. 164506.
- [20] B. Dünweg and K. Kremer. “Molecular dynamics simulation of a polymer chain in solution”. *J. Chem. Phys.* 99 (1993), pp. 6983–6997.
- [21] I.-C. Yeh and G. Hummer. “System-Size Dependence of Diffusion Coefficients and Viscosities from Molecular Dynamics Simulations with Periodic Boundary Conditions”. *J. Phys. Chem. B* 108 (2004), pp. 15873–15879.
- [22] T. Morawietz, A. Singraber, C. Dellago, and J. Behler. “How van der Waals interactions determine the unique properties of water”. *Proc. Natl. Acad. Sci. USA* 113 (2016), pp. 8368–8373.
- [23] P. Simonnin, B. Noetinger, C. Nieto-Draghi, V. Marry, and B. Rotenberg. “Diffusion under Confinement: Hydrodynamic Finite-Size Effects in Simulation”. *J. Chem. Theory Comput.* 13 (2017), pp. 2881–2889.
- [24] D. Chandler. *Introduction to Modern Statistical Mechanics*. Oxford University Press, Oxford, New York, Toronto, 1987.
- [25] D. Laage and J. T. Hynes. “On the Residence Time for Water in a Solute Hydration Shell: Application to Aqueous Halide Solutions”. *J. Phys. Chem. B* 112 (2008), pp. 7697–7701.
- [26] S. Imoto, H. Forbert, and D. Marx. “Water structure and solvation of osmolytes at high hydrostatic pressure: pure water and TMAO solutions at 10 kbar versus 1 bar”. *Phys. Chem. Chem. Phys.* 17 (2015), pp. 24224–24237.
- [27] P. Schienbein and D. Marx. “Liquid-Vapor Phase Diagram of RPBE-D3 Water: Electronic Properties along the Coexistence Curve and in the Supercritical Phase”. *J. Phys. Chem. B* 122 (2018), pp. 3318–3329.
- [28] P. Schienbein and D. Marx. “Assessing the properties of supercritical water in terms of structural dynamics and electronic polarization effects”. *Phys. Chem. Chem. Phys.* 22 (2020), pp. 10462–10479.
- [29] R. Kumar, J. R. Schmidt, and J. L. Skinner. “Hydrogen bonding definitions and dynamics in liquid water”. *J. Chem. Phys.* 126 (2007), p. 204107.
- [30] A. Luzar and D. Chandler. “Hydrogen-bond kinetics in liquid water”. *Nature* 379 (1996), pp. 55–57.